

Department of Physics and Astronomy  
University of Heidelberg

Bachelor Thesis in Physics  
submitted by

**Patrick Friebel**

born in Bruchsal (Germany)

**2017**



# Grating Alignment using Mach-Zehnder Interferometers

This Bachelor Thesis has been carried out by Patrick Friebel at the  
Kirchhoff Institute in Heidelberg  
under the supervision of  
Prof. Dr. M. K. Oberthaler



## Abstract

AtliX (Antiproton Talbot-Lau Interferometry eXperiment) aims at testing the wave nature of antiprotons. Proton interferometry acts as an intermediate step towards this goal. The device of choice is a Talbot-Lau interferometer, consisting of three equidistant transmission gratings. Misalignments in the order of tens of  $\mu\text{rad}$  will wash out the interference pattern. Therefore precise control of the mutual angle between the gratings is required.

Here, a concept using three independent Mach-Zehnder interferometers provides a means to monitor the angular differences. Two designs are detailed. One acts as a proof of principle using only two independent interferometers. The second one makes use of translational stages to implement all required beams. The results obtained in this work include characterization of the main components. A discussion on the signal shape and the methods to extract the phase information follow. Lastly the minimal detected resolution is given and compared to the critical angle for the Talbot-Lau interferometer.

AtliX (Antiproton Talbot-Lau Interferometry eXperiment) hat zum Ziel, die Welleneigenschaft von Antiprotonen zu testen. Protoninterferenz handelt als Zwischenschritt in diese Richtung. Das verwendete Gerät ist ein Talbot-Lau Interferometer, das aus drei äquidistanten Transmissionsgittern besteht. Abweichungen in der Größenordnung von zehn  $\mu\text{rad}$  verwaschen das Interferenzmuster. Deswegen ist präzise Kontrolle über den gegenseitigen Winkel zwischen den Gittern erforderlich.

Hier gibt ein Konzept, das drei unabhängige Mach-Zehnder Interferometer verwendet, Aufschluss über Winkeldifferenzen. Zwei Designs sind im Detail erklärt. Das Erste ist ein Machbarkeitsbeweis, das nur zwei unabhängige Interferometer verwendet. Das Zweite benutzt lineare Aktuatoren um alle benötigten Strahlen zu implementieren. Die Ergebnisse dieser Arbeit beinhalten eine Charakterisierung der Hauptkomponenten. Es folgt eine Diskussion über die Signalform und die Methoden zur Phasenmessung. Zum Schluss wird die minimale gemessene Auflösung angegeben und mit dem kritischen Winkel des Talbot-Lau Interferometers verglichen.



# Contents

<b>1</b>	<b>Introduction</b>	<b>6</b>
<b>2</b>	<b>Antiproton Interference In AtliX</b>	<b>8</b>
2.1	Experimental Principle . . . . .	8
2.2	Characteristics Of The Source . . . . .	9
2.3	Challenges . . . . .	10
<b>3</b>	<b>Theory</b>	<b>12</b>
3.1	Interferometry . . . . .	12
3.1.1	Fabry-Pérot Interferometer . . . . .	14
3.1.2	Michelson Interferometer . . . . .	14
3.1.3	Talbot-Lau Interferometer . . . . .	15
3.2	Mach-Zehnder In General . . . . .	16
3.3	The Three-Beam-Mach-Zehnder Interferometer . . . . .	18
<b>4</b>	<b>Experimental Realization</b>	<b>24</b>
4.1	Actuators . . . . .	24
4.2	Gratings . . . . .	25
4.3	Laser System . . . . .	27
4.4	Set-Up . . . . .	27
4.4.1	Proof Of Principle . . . . .	28
4.4.2	Variable System With Actuators . . . . .	29
<b>5</b>	<b>Results</b>	<b>32</b>
5.1	Testing The Actuators . . . . .	32
5.2	Shaping The Signal . . . . .	34
5.3	Monitoring The Tilt . . . . .	35
<b>6</b>	<b>Summary &amp; Outlook</b>	<b>44</b>
6.1	Summary . . . . .	44
6.2	Outlook . . . . .	44





# 1 Introduction

The wave nature of matter has been predicted by de Broglie [1]. Successful demonstrations were given with electrons [2], atoms [3] and molecules [4]. Antimatter is expected to follow the same principle. The AtliX project [5] (Antiproton Talbot-Lau Interferometry eXperiment) aims at demonstrating this with antiprotons at CERN. As an intermediate step AtliX aims to show interference with protons in Heidelberg. A Talbot-Lau interferometer is a proven tool for matter wave interference [6] [4] [7]. It was introduced by Ernst Lau in 1948 [8] and used with different particle species since then. In combination with the moiré effect, proton interference measurements are possible. The setup in AtliX consists of three equidistant transmission gratings and a position sensitive detector.

When using nanometric gratings, misalignments in the order of tens of  $\mu\text{rad}$  will wash out the interference pattern. Therefore controlling the angular positions is crucial. This thesis will outline a method to monitor angular differences between three equidistant gratings by means of laser interferometry. Three independent Mach-Zehnder interferometers make precise control of relative angles possible. Phase differences between the outputs are directly related to angular differences between the gratings. Similar experiments in the past have successfully employed this technique before [9] [10]. Here, a prototype for the conditions in AtliX is designed and tested.

The chapters are organized in the following structure:

Chapter two gives details on AtliX and (anti-)proton interferometry.

Chapter three discusses the theory of interferometry. It begins with a short introduction to interferometry in general before giving details on the three-beam Mach-Zehnder.

Chapter four focuses on the experimental realization. The main components for the project are introduced. These are the actuators, used to control the grating motion, the gratings and the laser system. Two setups are detailed.

The first acts as a proof of principle for the concept. The second is the full device using translational stages.

Chapter five gives the results of the experiment. Characteristics of the actuators are measured. A discussion on the signal shape follows. The main part of this chapter are the results of the angular measurements. The methods of phase extraction are discussed. This chapter concludes with the minimal achieved angular resolution in comparison to the desired one.

Chapter six concludes this thesis. It gives a summary of the work presented and an outlook into the next steps necessary to implement this concept AtliX.

## 2 Antiproton Interference In AtliX

This section will give an outline of the antiproton interference experiment in the scope of AtliX. It aims at giving the motivation behind the work towards grating alignment. This includes an introduction to AtliX. The focus is on antiproton interferometry with a device called Talbot-Lau interferometer. The critical angle associated with the experimental setup is given as the goal for this work.

### 2.1 Experimental Principle

AtliX (Antiproton Talbot-Lau Interferometry eXperiment) is meant to test the wave nature of antiprotons and, as an intermediate step, of protons. Experimentally this is achieved by a device known as Talbot-Lau interferometer. AtliX is a side project of AEGIS<sup>1</sup> (Antimatter Experiment: Gravity, Interferometry, Spectroscopy) whose goal is to test the weak equivalence principle by measuring the gravitational force on antimatter.

The Talbot-Lau interferometer [13] is based on observations by Talbot in 1836 [14] and Lau in 1948 [8]. Three equidistant gratings of periodicity  $d = 258$  nm form an interferometer based on the Talbot- and moiré effect. Grating one and two form a 'microscopic' fringe pattern of the grating periodicity  $d$  based on the Talbot-effect. Further detail can be found in section 3.1.3. The third grating is used as a mask for this fringe pattern. A tilt between the 'microscopic' fringes and the grating slits gives rise to a 'macroscopic' fringe structure based on the moiré effect. Figure 2.1 shows an example. Here, proof for the quantum character of the used particles is given by the visibility profile  $\nu$  (often referred to as 'contrast') of the measured fringes

$$\nu = \frac{I_{\max} - I_{\min}}{I_{\max} + I_{\min}} . \quad (2.1)$$

---

<sup>1</sup>Further information about the experiment can be found in [11] [12]

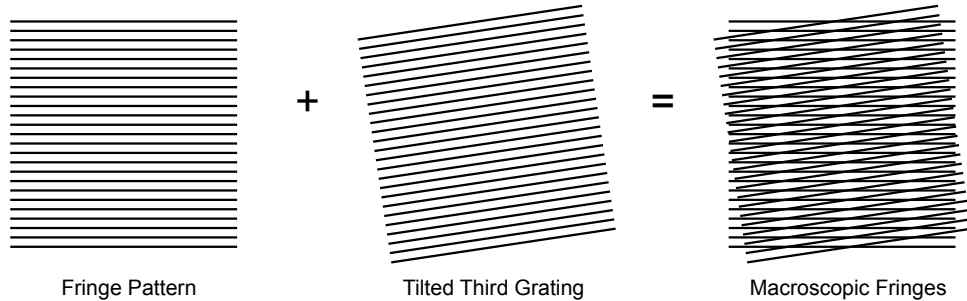


Figure 2.1: Moiré effect. The interference pattern is superimposed by a tilted grating of same periodicity. The resulting macroscopic fringes are recorded by a spatially resolving detector.

Different to the classical case,  $\nu$  depends on the mean particle energy if operated in the wave regime. Figure 2.2 shows the behavior for the conditions in AtliX. Put together, this forms an interferometer that has two advantages: Firstly, it can operate with a diffusive source. And secondly, the 'macroscopic' fringes after the interferometer do not require a high resolution detector to be recorded.

## 2.2 Characteristics Of The Source

The antiprotons are provided by the Antiproton Decelerator (AD) at CERN. They are created by a pair production process. The antiprotons exit the decelerator in bunches of  $10^7$  approximately every 100 s. Their mean energy is 5.3 MeV. At this energy the silicon gratings become transparent. The project is envisioned to operate in a range between  $E = 1 \text{ keV} - 10 \text{ keV}$ . Therefore a degrader foil together with a selection process for the low energy antiparticles is needed. The result is a drastic decrease in flux to 30 antiprotons per shot with a broad energy spectrum, which is insufficient for commissioning the device.

In order to study the systematics of the experiment, as an intermediate step AtliX is planned to perform Talbot-Lau interferometry with protons.

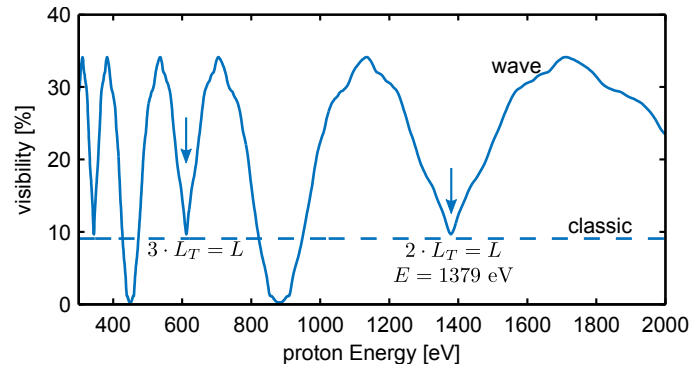


Figure 2.2: Visibility of the interference pattern as a function of proton energy. In the wave regime, the visibility changes drastically with particle energy. For the classical case, no change in visibility is expected. Courtesy of A. Demetrio [15].

Protons and antiprotons show the same behavior when exposed to electric and magnetic fields (with an opposite charge) and can be easily produced throughout standard plasma sources. Furthermore, reproducible results on proton interference do not exist.

The experimental setup in Heidelberg makes use of a tunable ECR proton source [16] with an operating flux of the order of  $10^5$  particles per second. The source emits a beam of particles in the energy range between 500 eV and 2 keV, with a 1 % monochromaticity. Relying on a setup operated in controlled conditions and independent on AD beam time makes the development of the device considerably easier.

### 2.3 Challenges

AtliX is sensitive to several effects. Charge up in the setup leads to electric and magnetic stray fields, thus disturbing the measurement. Any non conductive elements, such as the gratings, must be metal coated. To reduce the influence from external magnetic fields, a mu-metal shield surrounds the setup. With a relative permeability in the order of  $\mu_r = 100\,000$ , this alloy guides external magnetic fields inside itself. It also acts as a Faraday cage. Secondly, vibrations of the order of  $d$  between the gratings wash out the fringe pattern, thus

destroying the measurement. To mitigate vibration, both the gratings and the position sensitive detector are mounted on a single aluminium block. Lastly, the relative angle between the gratings must be controlled. For low flux, as is expected with antiprotons, angular changes during the integration time washes the pattern out. Furthermore, one wants to know beforehand what the relative angular position of each grating is. The moiré pattern is dependent on the angle between the microscopic fringes and the slits of the third grating. With a grating periodicity of  $d = 258 \text{ nm}$  and a grating width of  $b = 7 \text{ mm}$ , for every angular difference of

$$\Delta\alpha_{\text{crit.}} = \frac{d}{b} = 37 \text{ } \mu\text{rad} \quad (2.2)$$

one more macroscopic fringe appears. The angular relationship between the pattern and the third grating gives the number of expected fringes. Also differences between grating one and two can potentially wash out the interference pattern created by the Talbot-effect.

The work presented in this thesis is focused on an experimental method to control the angular relationship between the gratings. A system of three independent Mach-Zehnder interferometers is supposed to make measurements of angular differences possible. This technique found use in similar applications [9], [17]. Throughout this thesis, a prototype outside the vacuum will be tested. A means to measure tilts independently and precisely would advance the experiment towards antiproton interferometry.

## 3 Theory

This chapter provides the theoretical background for the three-beam Mach-Zehnder interferometer. The interferometer is a tool used to monitor the alignment of three equidistant gratings. A short summary on interferometry is provided before discussing examples. This includes the Talbot-Lau and the Mach-Zehnder interferometer. The chapter concludes with a description of the three-beam Mach-Zehnder interferometer.

### 3.1 Interferometry

The dictionary “Merriam Webster’s” defines the term interferometer as “an apparatus that utilizes the interference of waves (as of light) for precise determinations (as of distance or wavelength)”[18]. This is a very broad definition but it describes the process that is known as interferometry very well.

Interference has been known since Thomas Young’s double slit experiment in 1801 in which he illuminated two slits with the same light source and observed the famous interference pattern behind it. The interferometers that have been developed since then got increasingly sophisticated and precise.

If two waves are superimposed the resulting pattern is given by the intensity of the field, which is not directly the sum of the fields. Furthermore, the waves can’t be generic: they have to have the same polarization and the same wavelength, otherwise no interference pattern can be seen. This formation of characteristic patterns is known as constructive and destructive interference. For light the equivalent is the superposition of electric  $E_i$  and magnetic  $B_i$  fields. Since the intensity  $I$  is given by the temporal average of the square of the electric field<sup>2</sup>  $E(t)$ .

$$I \sim \langle \mathbf{E}^2(\mathbf{r}, t) \rangle_T = \langle \mathbf{E}_0^2 \cos^2(\mathbf{k} \cdot \mathbf{r} - \omega t + \delta) \rangle_T \quad (3.1)$$

---

<sup>2</sup>vectors are written as  $\vec{a} = \mathbf{a}$

### 3 Theory

---

In experiments not the electric field is measured but the intensity of the light. So if one has a superposition of two fields  $E_1$  and  $E_2$  the observed intensity becomes

$$\mathbf{E}^2 = \mathbf{E}_1^2 + \mathbf{E}_2^2 + 2\mathbf{E}_1\mathbf{E}_2 \quad (3.2)$$

$$I = I_1 + I_2 + I_{12} . \quad (3.3)$$

The last term is identified as the interference term

$$I_{12} = 2\langle\mathbf{E}_1\mathbf{E}_2\rangle_T , \quad (3.4)$$

with

$$\langle\mathbf{E}_1\mathbf{E}_2\rangle_T = |E_1| |E_2| \cos(\delta) \quad (3.5)$$

for sufficiently large integration time  $T$ .  $\delta$  denotes the phase difference. The total intensity is given by

$$I = I_1 + I_2 + 2\sqrt{I_1 I_2} \cos(\delta) . \quad (3.6)$$

For equal intensities  $I_1 = I_2 = I_0$  one finds

$$I(\delta) = 2I_0(1 + \cos \delta) = 4I_0 \cos^2\left(\frac{\delta}{2}\right) . \quad (3.7)$$

The phase shift  $\delta$  can be expressed as a function of the wavelength  $\lambda$  as

$$\delta = 2\pi \frac{d}{\lambda} , \quad (3.8)$$

where  $d$  is the optical path difference between the two waves. Thus, by measuring  $\delta$ , one can calculate path differences with high accuracy. This is the essence of interferometry [19] [20] and is used in many different applications. The most prominent ones will be detailed now.



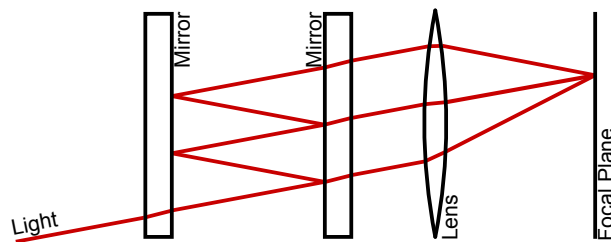


Figure 3.1: Schematic of the Fabry-Pérot interferometer. Light entering experiences multiple reflections. At every turn a fraction leaves the device. A lens focuses the light in its focal plane where the beams interfere.

### 3.1.1 Fabry-Pérot Interferometer

The Fabry-Pérot-Interferometer [20] has been designed by Charles Fabry and Alfred Pérot in 1897. It consists of two semitransparent mirrors placed at distance  $d$ . This setup can be used with an extended light source, often in combination with a lens. Light enters the device under an angle  $\Theta$  and experiences multiple reflections inside with a fraction leaving on every turn. A lens behind the device is bringing the output beams to a common focus where they interfere. Changing the distance between the mirrors affects the phase difference between each reflected beam.

The Fabry-Pérot is more commonly used as an optical resonator because of its great spectral resolution.

### 3.1.2 Michelson Interferometer

Introduced by Michelson, this type of interferometer is best known for an experiment in 1887, when Michelson and Morley [21] used a version of it to measure the constant nature of the speed of light. More recently a large scale Michelson-Interferometer *LIGO* [22] reported success in the detection of gravitational waves.

The Michelson-interferometer consists of two mirrors, a beam splitter, and a monochromatic light source as shown in figure 3.2. The beam splitter divides the beam into two paths, leading to mirrors with ideally 100% reflectivity.

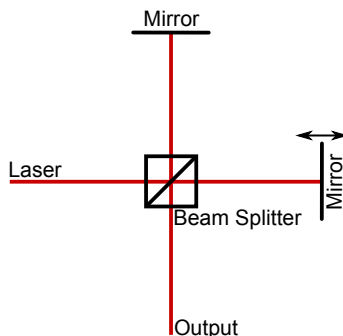


Figure 3.2: Schematic of a Michelson interferometer. The light is split by a beam splitter. Two mirrors reflect the arms back. The splitter recombines both arms. The signal depends on the path difference.

A difference in length between the two paths generates a phase shift in the observed light pattern. Equal distance gives constructive interference and a difference in distance of  $\Delta x = (2m + 1)\frac{\lambda}{4}$ , where  $m \in \mathbb{Z}$ , gives destructive interference.

### 3.1.3 Talbot-Lau Interferometer

The Talbot-Lau-interferometer [13][15] is at the heart of the AtliX experiment. It can be seen as the quantum-mechanical counterpart of the Moiré-Deflectometer in which classical particle paths are considered.

The Talbot-effect [14], named after H. F. Talbot in 1836, describes how a plane wavefront with wavelength  $\lambda$  transmitted through a grating with periodicity  $d$  gives a characteristic structure in regular intervals. This is valid for the near field regime. At integer multiples of the so called Talbot-length

$$L_T = \frac{d^2}{\lambda} \quad (3.9)$$

a fringe pattern of period  $d$  builds up. For fractions of  $L_T$  a pattern of higher periodicity is observable. This structure is called 'Talbot carpet'. For a diffusive wavefront the pattern washes out and the fringe visibility  $\nu$  goes to zero. E. Lau [8] showed in 1948 that this problem can be circumvented by

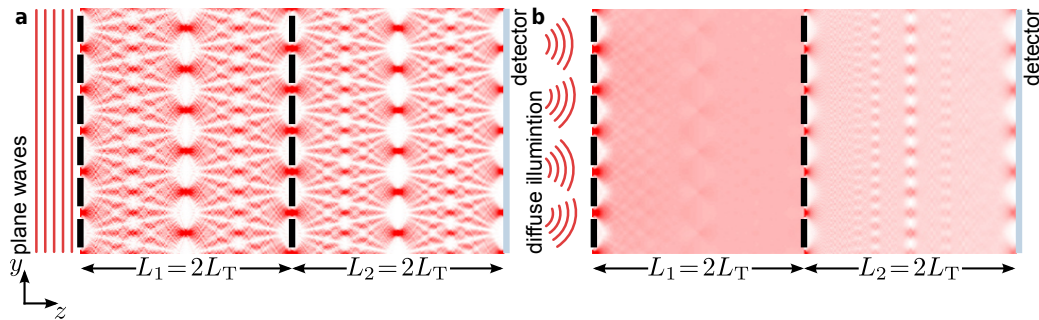


Figure 3.3: a. Talbot carpet produced by a plane wave impinging on a grating. Self imaging of the gratings occurs at integer multiples of  $L_T$ ; b. For a diffusive source the first grating creates spacial coherence at the second grating. An interference pattern is measured in the detector plane. Courtesy of P. Bräunig [13].

using a second grating. Here the first grating creates coherence at multiple of  $L_T$  where grating two is placed. Therefore in the detector plane at the same distance from grating two the same fringe pattern is observed as in the case of plane waves. Figure 3.3a. shows the Talbot-Lau interferometer with plane waves and 3.3b. with a diffusive source.

### 3.2 Mach-Zehnder In General

Ludwig Mach [23] and Ludwig Zehnder [24] introduced the concept that is now known as the Mach-Zehnder interferometer independently in 1892 and 1891 respectively. Even though the most commonly used setup consists of beam splitting cubes and mirrors the underlying idea is very generic: Split a light beam into two equally long arms and recombine them. This is also known as amplitude splitting. An optical path difference introduced in one of the arms has then an effect on the output.

The two different Mach-Zehnder interferometer are now discussed in detail.

- **Splitting via cubes:**

This method is the most commonly used. Splitting and recombination

of the beam is done by beam splitting cubes while mirrors are used to guide the beams. A simple sketch of the most general setup can be found in figure 3.4a. The beam paths ideally create a parallelogram which keeps both arms equally long. An optical path difference introduced in one of the arms leads to a phase shift in comparison with the other arm. For instance, placing a target of optically transparent material with refraction index  $n \neq 1$  in one arm will cause a phase shift proportional to the depth of the target. In this setup one finds two outputs where the signal is modulated by  $\sim \cos^2(\frac{\delta}{2})$  and  $\sim \sin^2(\frac{\delta}{2})$  respectively (see figure 3.4a.).

The particular design of the Mach-Zehnder setup with its separated arms has the advantage that it can be scaled to desired proportions. This type of interferometer often finds use in plasma diagnostics [25] and wind flow studies [26].

- **Splitting via gratings:**

This type of Mach-Zehnder interferometer uses diffraction gratings for both beam splitting and guiding. Three gratings are placed directly behind each other and the beam is traveling through them experiencing diffraction. In the simple picture with two arms one considers the zeroth and first order from the first grating and the first and minus first order respectively after the second grating. The third grating recombines both arms again (See figure 3.4b.). In analogy to the case above one can find two equivalent outputs. But in contrast the output is dependent on the type of grating used. When using phase gratings, the two output signals are proportional to  $\sim \cos^2(\frac{\delta}{2})$  and  $\sim \sin^2(\frac{\delta}{2})$ , while for amplitude gratings the outputs show the same behavior  $\sim \cos^2(\frac{\delta}{2})$ .

The Mach-Zehnder interferometer consisting of gratings falls in the category of a white light interferometer, since this type of interferometer works over a long bandwidth of optical frequencies. For gratings this is true since only the diffraction angle depends on the frequency. Every

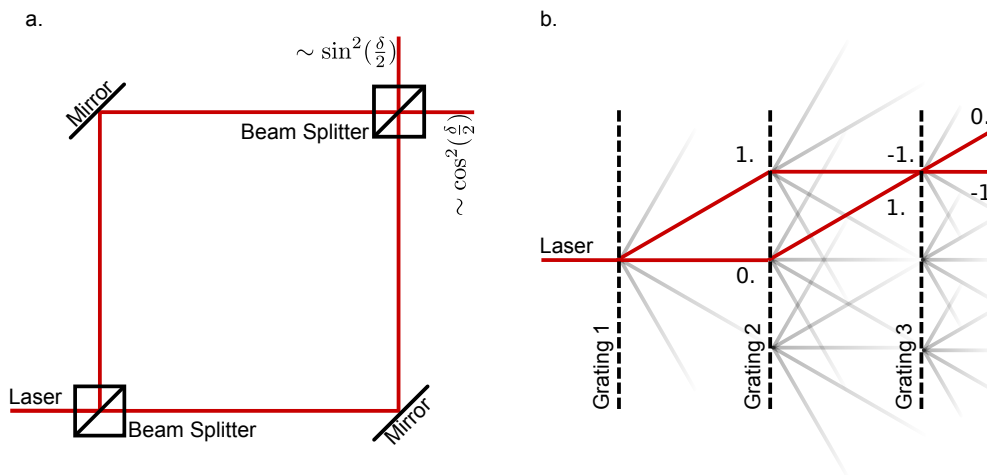


Figure 3.4: Mach-Zehnder interferometers. a. beam splitting is done by beam splitter cubes. The two arms are guided by mirrors and recombined by another cube. b. diffraction gratings split, guide and recombine the light.

wavelength interferes in a different position on the third grating.

The wave nature of particles allows this interferometer type to be used to test particle interference. As an example neutron interferometry has been realized using this type of interferometer [9].

### 3.3 The Three-Beam-Mach-Zehnder Interferometer

This concept can be found in similar applications in work on neutron interferometry[9] and in theses from M. Weber[10] and G. Van der Zouw[27].

The Mach-Zehnder interferometer has been used to monitor mechanical stability and vibrations of different systems, due to the accuracy achieved by carefully choosing the wavelength and the geometry of the device. Previous work in in this group used a set up of two Mach-Zehnder interferometers to monitor the stability of a grating deflectometer [28].

Here, a design is discussed which is suitable to measure the relative angles between the gratings of a Talbot-Lau interferometer. The device consists of three independent Mach-Zehnder interferometers, whose outputs can be used to determine the orientation of the single gratings with an expected accuracy

of less than the critical  $37 \mu\text{rad}$  for the Talbot-Lau interferometer in AtliX. The theoretical description of the three-beam Mach-Zehnder interferometer is based on the Fourier framework of diffraction. The Fourier character of Fraunhofer diffraction introduces the effect of phase shifts given by translation of the aperture. Since the length of the slits is significantly bigger than the beam size it is sufficient to discuss only the one dimensional transformation. The Fourier transform is defined as

$$\mathcal{F}[f(x)] = \int_{-\infty}^{\infty} f(x)e^{i2\pi kx} dx . \quad (3.10)$$

A translation of the original function introduces the phase shift  $\Phi$

$$f(x) \longrightarrow f(x - a) \Rightarrow \mathcal{F}[f(x)] \longrightarrow e^{i\Phi(a)} \mathcal{F}[f(x)] . \quad (3.11)$$

A measurements of phase differences is possible by interference. This concept is at the core of the grating Mach-Zehnder.

In order to extract this information, it is necessary to estimate the difference in phase between the two paths of the interferometer.

For a grating with periodicity  $d$  the phase factor introduced in equation 3.11 is left invariant under a translation  $\Delta t_i = d$ , in which the index  $i$  refers to the grating,

$$\Delta\Phi = \frac{2\pi}{d}(n_1\Delta t_1 + n_2\Delta t_2 + n_3\Delta t_3) , \quad (3.12)$$

where  $n_i \in \mathbb{N}$ . Shifting all gratings by the same arbitrary amount  $\Delta t_i$  must leave the phase unchanged

$$\Delta\Phi = 0 \longrightarrow n_1 + n_2 + n_3 = 0 \quad (3.13)$$

and shifting only grating 1 or 3 must have the same effect for symmetry reasons

$$n_1 = n_3 . \quad (3.14)$$

One finds the sensitivity of the Mach-Zehnder interferometer to an arbitrary set of translations  $\Delta t_i$  to be[27]

$$\Phi = \frac{2\pi}{d} (\Delta t_1 - 2\Delta t_2 + \Delta t_3) . \quad (3.15)$$

One can also retrieve the same result by using the properties of the Fourier transform. In particular, the phase shift is dependent on the  $n^{\text{th}}$  order of diffraction via

$$\Phi_n = 2\pi n \frac{\Delta t_i}{d} . \quad (3.16)$$

In order to get the phase in the resulting output one takes the phase accumulated in both arms and calculates the difference

$$\begin{aligned} \Phi_{\text{total}} &= (\Phi_1 + \Phi_{-1} + \Phi_0)_{\text{Arm2}} - (\Phi_0 + \Phi_1 + \Phi_{-1})_{\text{Arm1}} \\ &= \frac{2\pi}{d} (\Delta t_1 - \Delta t_2 + 0 \cdot \Delta t_3)_2 - \frac{2\pi}{d} (0 \cdot \Delta t_1 + \Delta t_2 - \Delta t_3)_1 \\ &= \frac{2\pi}{d} (\Delta t_1 - 2\Delta t_2 + \Delta t_3) . \end{aligned} \quad (3.17)$$

This is the same relation as derived above.

A small tilt by the angle  $\alpha$  manifests itself by  $\Delta t_i = \alpha_i y_i$  where  $y_i$  is the respective position on the grating along the slits. This  $y_i$  will later be the distance between two parallel beams.

$$\Phi = \frac{2\pi}{d} (\alpha_1 y_1 - 2\alpha_2 y_2 + \alpha_3 y_3) \quad (3.18)$$

The following setup takes advantage of this phase behavior to monitor the tilts:

Two parallel ('straight') Mach-Zehnder beams are traveling through the grating with a separation distance  $h$ . One straight interferometer will give the zero position in  $y_i = 0$ . In these coordinates the other straight beam is in position  $y_i = h$ . A third angled Mach-Zehnder beam is aligned such that

### 3 Theory

---

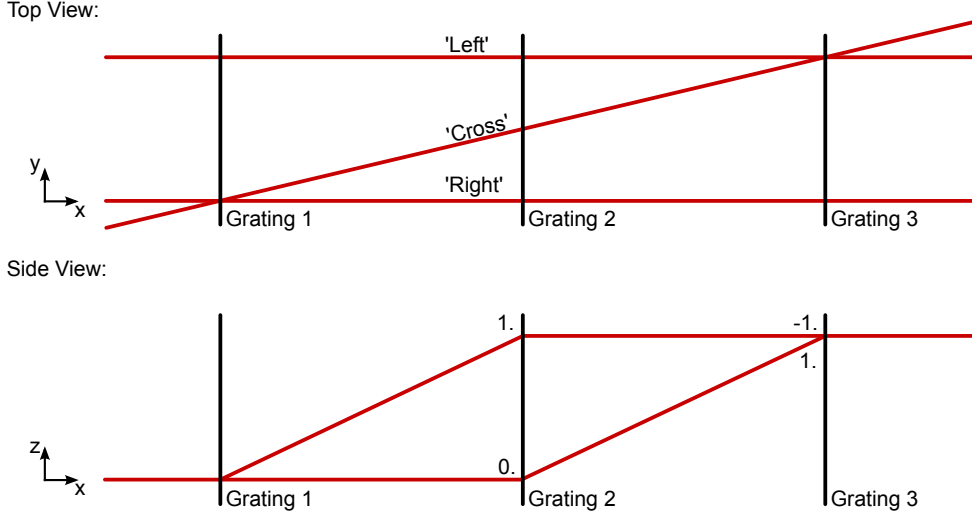


Figure 3.5: Geometry of the setup. Top view: 'Left' and 'Right' interferometer are parallel with distance  $h$ . 'Cross' intersects the 'Right' beam at grating one and the 'Left' beam at grating three. Side view: Arms of the grating Mach-Zehnder. Grating one and two rotate around the x-axis; grating three translates in z-direction.

it intersects one straight beam in the plane of grating one and the other in the plane of grating two (see figure 3.5). By choosing this geometry one can eliminate  $y_2$  with

$$y_2 = \frac{y_1 + y_3}{2} \quad (3.19)$$

This reduces the expression for the phase between the interferometers to

$$\Phi = \frac{2\pi}{d} [(\alpha_1 - \alpha_2) y_1 + (\alpha_3 - \alpha_2) y_3] \quad (3.20)$$

Note that this expression is only dependent on the periodicity of the gratings and the spacial separation of the Mach-Zehnder interferometers. The only constraint on the distance between the gratings (besides being equidistant) is to be in the far field regime for Fraunhofer diffraction. This is a 'soft' constraint since beyond this regime the grating distance  $L$  can be chosen freely.

The three beams are denoted as 'Right', 'Left', and 'Cross'. One straight



### 3 Theory

---

beam is taken as reference ( $y_1 = y_3 = 0$ ) with arbitrary phase  $\Phi_{Offset}$ . The other two phases are then known as:

$$\Phi_{Right} = \Phi_{Offset} \quad (3.21)$$

$$\Phi_{Cross} = 2\pi \frac{h}{d} (\alpha_3 - \alpha_2) + \Phi_{Offset} \quad (3.22)$$

$$\Phi_{Left} = 2\pi \frac{h}{d} [(\alpha_1 - \alpha_2) + (\alpha_3 - \alpha_2)] + \Phi_{Offset} \quad (3.23)$$

By taking the phase differences one can retrieve angular differences between the gratings

$$\Phi_{Left} - \Phi_{Cross} = 2\pi \frac{h}{d} (\alpha_1 - \alpha_2) \quad (3.24)$$

$$\Phi_{Cross} - \Phi_{Right} = 2\pi \frac{h}{d} (\alpha_3 - \alpha_2) \quad (3.25)$$

One sees that one full phase shift of  $\Delta\Phi = 2\pi$  corresponds to an angular difference of  $\Delta\alpha = \frac{d}{h}$ . This means that the angular sensitivity in general can be adjusted by choosing the parameters  $d$  and  $h$  to the needed conditions. For a maximal sensitivity on the angles measured, the distance between the two straight Mach-Zehnder interferometers is kept as large as possible.

The maximum phase shift that can be resolved is limited to  $2\pi$ . Therefore, bigger shifts can't be properly recognized. This means that this method is best suited for precision monitoring/alignment that needs to be complemented with a second rough monitoring method.

In order to measure the phase differences introduced by relative tilts of the gratings one of the three gratings is shifted in a direction perpendicular to the grating vector. A movement  $\Delta z = d$  is needed to record a full modulation. The phase shift recorded can be then translated to a relative angular difference between the scanned grating and the other two, as expressed in Eq. (3.24) and (3.25). If grating three is scanned linearly the tilt of grating two is given in relation to grating three and then grating one in relation to grating two.



## 4 Experimental Realization

This section gives a description of the experimental setup shown in figure 4.2 and 4.3. The main component are introduced in the following subsections. The actuators are in place to tilt grating one and two and to linearly move grating three in z-direction. These diffraction gratings provide the basis for the Mach-Zehnder interferometers. A Helium-Neon laser provides the coherent light for this experiment. The chapter concludes with a discussion of the initial and the improved designs of the setups.

### 4.1 Actuators

Three actuators provide the ability to move the gratings in rotational and straight direction. Grating three is mounted on a linear actuator while grating one and two are mounted on goniometers. The actuators are manufactured by *attocube systems AG* [29] in Munich. Their original working environment is the main experiment in AtliX. The important parameters for this work are listed in Table 4.1 and 4.2. The input and readout electronics is provided by *attocube* as well. A linear continuous scanning mode is not available. It

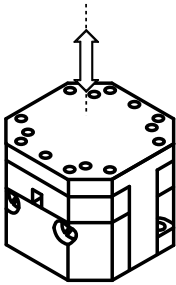
ANPz101 RES		
	Parameter	Value
	footprint; height	$24 \times 24$ ; 20 mm
	travel range	5 mm
	fine pos. range at 300K	$5 \mu\text{m}$
	step size repeatability	typ. 5 %
	readout mechanism	resistive sensor
	sensor resolution	approx. 200 nm
	repeatability	$1-2 \mu\text{m}$

Table 4.1: Parameter table for the linear positioner ANPz101 RES in z-direction manufactured by *attocube* [29]

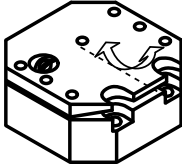
ANGt101 RES		
	Parameter	Value
	footprint; height	$24 \times 24$ ; 11 mm
	travel range	0.115 rad
	step size repeatability	typ. 5 %
	step asymmetry	typ. 5 %
	readout mechanism	resistive sensor
	sensor resolution	approx. $1.7 \mu\text{rad}$
	repeatability	$35 \mu\text{rad}$

Table 4.2: Parameter table for the goniometer ANGt101 RES manufactured by *attocube* [29]

is possible to go continuously to a position but this is highly nonlinear in velocity. For this work this means step by step scanning will be used. The linear actuator can be reliably used down to a steps size of  $0.5 \mu\text{m}$  while the goniometers have a minimal reliable angular step size of  $35 \mu\text{rad}$ .

With the goniometers the group has observed a discrepancy between the applied step size and the actual traveled range. A factor of 1.2 has been measured with simple tests described in section 5.1. That factor has to be accounted for in the read out.

In the linear actuator a hysteresis effect is observed. Details are described in section 5.1.

## 4.2 Gratings

Three diffraction gratings form the Mach-Zehnder interferometer. The gratings are produced out of a silicon wafer on which the pattern is printed by *Deep Reactive Ion Etching* (DRIE) [30]. This is a multi step process starting with covering the parts of the silicon waver that are not supposed to be etched with a mask. Then a plasma (of  $SF_6$  for silicon wavers) is accelerated onto the waver by applying an electric field starting the etching process. After

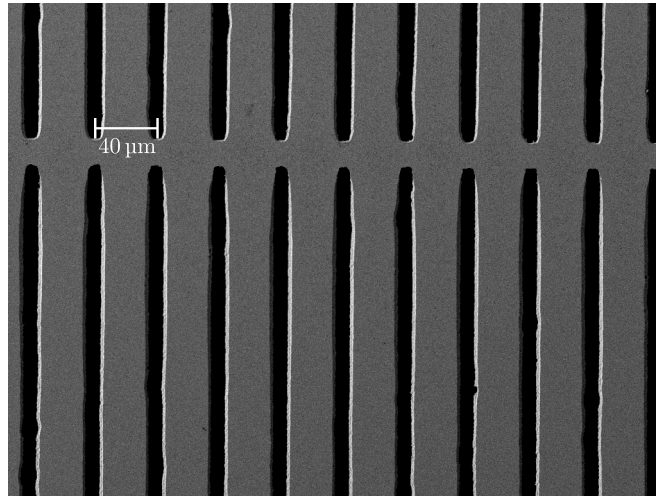


Figure 4.1: SEM picture (Scan Electron Microscopy) of the 40  $\mu\text{m}$  grating. The vertical black stripes are the slits. In gray structure is the silicon. Horizontally the support structure is visible. The measured open fraction is smaller than the nominal  $\eta = 30\%$  (SEM pictures courtesy of Lisa Veith and Anne Kast)

a short exposure time (several seconds) a polymer membrane is created by introducing a gas ( $C_4F_8$ ) into the plasma region that protects the walls in the etching areas. By alternating this method of etching and protection deep vertical valleys can be achieved. Out of this wafer pieces of area  $1\text{ cm} \times 1\text{ cm}$  are cut and glued on an aluminium support. The gratings have been coated with a gold/palladium alloy to prevent charging up of the underlying silicon. The diffraction gratings used in this work are transmission gratings of periodicity  $d = 40\ \mu\text{m}$ . The pattern is superimposed by a perpendicular support structure. These are bars of distance 2 mm that are supposed to stabilize the grating slits. This support structure does not have a significant effect on the diffraction of red laser light used here.

The open fraction  $\eta$  of the gratings was measured by 'SEM' [15] (Scanning Electron Microscopy) and by measuring the Talbot carpet [31] since it is critical to the fringe visibility in (anti-) proton interferometry.  $\eta$  is defined as the fraction of slit width  $b$  and grating periodicity  $d$ . The effective open fraction is between  $\eta = 14\%$  [15] and  $22\%$  [31] compared to the nominal

$\eta = 30\%$  [32] due to the production process.

Detailed information on the gratings and the development process can be found in the Phd. thesis of F. Hauptert [32].

### 4.3 Laser System

The light source is an intensity stabilized HeNe-laser. This laser provides 1 mW of power and a wavelength of  $\lambda = 633$  nm. In order to get the beam into position it is fiber coupled and ends in an adjustable focusing lens. The power output measured after the fiber exit is:

$$P = 330 \pm 5 \mu\text{W} . \quad (4.1)$$

One has to consider the power loss that occurs by having diffraction orders that are not relevant for the grating Mach-Zehnder. A simple measurement with a power-meter revealed that in the order of 1% of the incoming power is left in the output one is interested in.

### 4.4 Set-Up

This section discusses the experimental realization of the three-beam Mach-Zehnder. With the actuators, gratings and the laser described above two different designs are given.

The first setup was intended as a proof-of-principle, therefore one of the two parallel beams was omitted. As can be seen in equation (3.24) and (3.25) a simple setup can be designed only with one straight and the cross beam that gives the corresponding angular differences. Here, setting up only the 'Left' and the 'Cross' beam will give the angular difference between Grating 1 and 2.

The complete three beam interferometer for tilts is described afterwards, in section 4.4.2. As the available laser is too weak for the full three beam Mach-Zehnder the laser was motorized via linear actuators, thus simplifying the build but - at the same time - introducing systematic effects, which will

be discussed in Chapter 5.

#### 4.4.1 Proof Of Principle

A schematic of the setup is shown in Figure 4.2. The two beams originate from the same intensity stabilized HeNe-laser ( $\lambda = 633 \text{ nm}$ ) of random polarization that is fiber coupled into an adjustable focusing lens. The beams are then split in two by a polarizing beam splitting cube (note that the polarization is of no importance for the amplitude gratings used in this experiment). The beam going straight is the straight interferometer while the beam reflected by  $90^\circ$  is guided by a mirror in the 'Cross' position.

The gratings are mounted on aluminium supports which are fixed onto the piezo actuators. These are in turn mounted on an aluminium block from the AtliX main experiment. The block is designed for a distance between the gratings of  $L = 171.7 \text{ mm}$ . The distance between the gratings must be in the far field regime. This condition is valid when

$$\frac{d^2}{L\lambda} \ll 1 . \quad (4.2)$$

Here,  $d = 40 \text{ }\mu\text{m}$  is the aperture size and  $\lambda = 633 \text{ nm}$  is the wavelength. One finds a value of  $0.015 \ll 1$ , validating this condition.

In order to prevent more than two orders of diffraction from going through each grating, an aluminum aperture was placed in front of the gratings. Although this solution allowed for an easier beam selection, it led to unwanted multiple reflections, which distorted the signal shape. Replacing them with equivalent slits made of black cardboard 'cleans up' the signal completely. A detailed discussion is given in section 5.

The data is recorded by standard reverse biased photodiodes from *Thorlabs* (Model DET10A/M [33]). Due to space constraints of the work environment and the size of the package around the diodes a beam splitter or a mirror has to be placed inside the beam path to get the signal onto the active area of both diodes. Another Polarizing Beamsplitter Cube (PBC) has been chosen

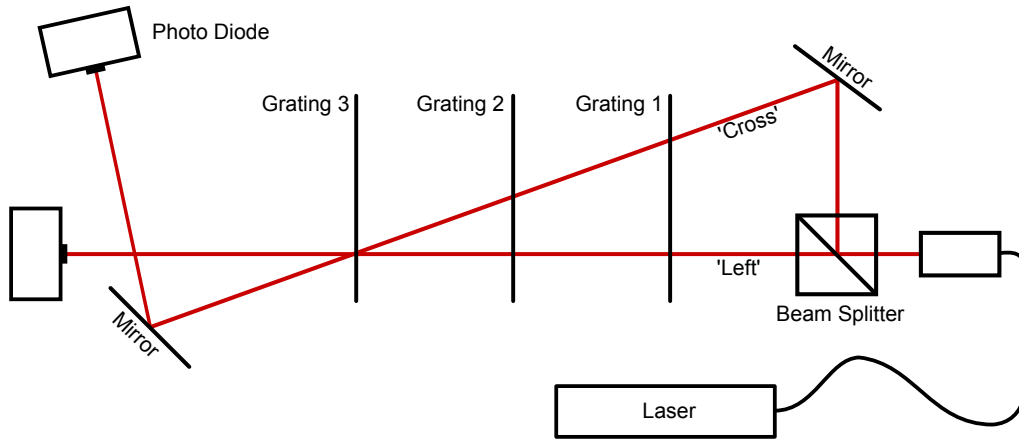


Figure 4.2: Setup to prove the basic concept. A HeNe laser is coupled to a fiber, split by a Polarizing Beamsplitter Cube and guided by mirrors into the 'Left' and 'Cross' positions on the gratings. The signal is recorded by two photodiodes. Due to space constraints the 'Cross' beam has to be reflected once more.

because it could be mounted to guide one beam without obstructing the other.

#### 4.4.2 Variable System With Actuators

A schematic of the setup is shown in figure 4.3. To build the full system with 3 Mach-Zehnder interferometers a design using translational stages is in place. Here the same HeNe-laser as mentioned above is used. Because the intensity in the previous build with the available laser was so low (order of magnitude  $1 \mu\text{W}$ ; see section 5) instead of splitting it into three parts, the full intensity is put into one Mach-Zehnder.

The idea is to move both the laser out coupler and one photodiode on two linear translational stages. A third linear actuator is used to tilt the laser out coupler into the 'Cross' position. These actuators of type *Oriel encoder mike* have a resolution of  $0.1 \mu\text{m}$  and a range of 51 mm which fits the requirements. This means the third grating needs to be scanned three times to make a statement on the angular differences between the gratings. The non reflective



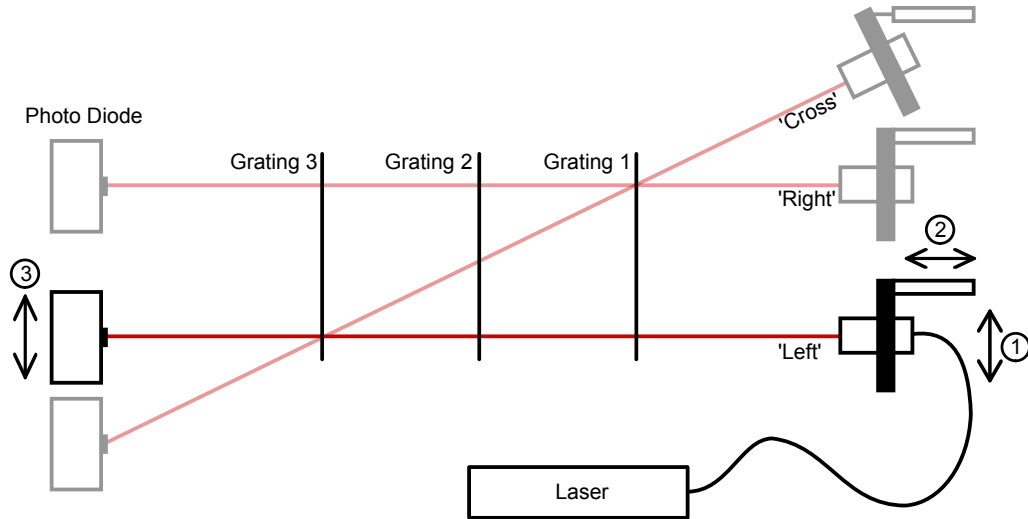


Figure 4.3: Set Up using linear actuators for translation of the laser out coupler and the photo diode. The tilt of the out coupler is given by a third linear actuator. Position of each Mach-Zehnder 'Left', 'Right' and 'Cross' in the gratings is recorded by the same Laser and photo diode. Operation of actuators: 1. parallel movement of laser; 2. tilt of laser; 3. parallel movement of photo diode

slits mentioned above are included in this setup. Another difference is, that the gratings have been moved from the aluminium block and placed with the actuators on an aluminum bar at a longer distance of  $L = 250$  mm. This made the positioning of the screens and the alignment of the photodiode simpler since the diffraction orders are spaced further apart. By equation 4.2 this distance is in the far field regime.

Only two of the *Oriel* actuators can be controlled simultaneously. One scan consists of three individual measurements with repositioning of the laser and the photo diode in between. The procedure is in order (see figure 4.3):

1. Movement of the laser parallel to the gratings
2. Tilt of the laser out coupler ('Cross'- or 'Straight'-position)
3. Movement of the photo diode parallel to the gratings. This position is

## 4 Experimental Realization

---

determined by observation of the output. It reaches its maximum if the laser is centered on the active area of the diode.

## 5 Results

The results obtained from the setups in chapter 4 are presented. Measurements on the hysteresis and correction factor for the actuators are detailed in section 5.1. Furthermore a discussion on the signal shape is found in section 5.2. Section 5.3 aims at giving the minimal resolved angular resolution. This includes comments on cross correlation and fitting of sine- and linear functions to the data for phase extraction. The relation between applied angle and measured angle serves as a means to verify the results.

### 5.1 Testing The Actuators

As discussed in section 4.1 the linear actuator shows hysteresis effects and the goniometer readout needs to be adjusted with a correction factor. These will be detailed in the following parts.

#### Linear Positioner

When reversing the direction of the linear actuator movement, one observes a discrepancy of the real position and the readout. This effect vanishes when moving in the new direction.

Figure 5.1 shows this effect in the given actuator by observation of the fringe pattern when scanning grating three. One full period must correspond to a movement of  $d = 40 \mu\text{m}$ . The blue curve is taken as reference over a long scan of  $(400 \mu\text{m})$ . The orange curve is supposed to be a repetition of the range between  $2200 \mu\text{m}$  to  $2400 \mu\text{m}$ . In the beginning of the scan a clear mismatch between the reference and the repeated scan is visible. By the end both signals are in phase. This effect can be attributed to hysteresis of the actuators. A counter strategy is to go further back and then move up to the desired position. At this point it will already have caught up and the signals match. It was found that going back by  $200 \mu\text{m}$  is sufficient to ensure the actuator reproducibility.

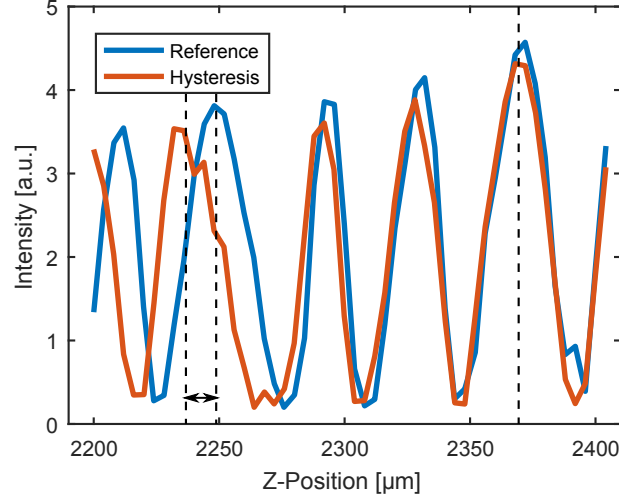


Figure 5.1: Hysteresis effect. The plot shows two scans of the same region. When changing direction of the linear actuator, hysteresis becomes visible. At first, the signal is out of phase. After approx. 200  $\mu\text{m}$  the signal stabilizes. As a counter measure, moving further back and forth before measurement eliminates the hysteresis effect. This phenomenon is reproducible.

## Goniometer

The Goniometers show a discrepancy between the applied angular step and the actual tilt. One finds a correction factor  $c_{cor.}$  of

$$\alpha_{\text{real}} = c_{cor.} \cdot \alpha_{\text{read out}} \quad (5.1)$$

$$c_{cor.} = 1.2 . \quad (5.2)$$

A first indication of this effect was found during the work presented here when the results obtained on the angular scans (see section 5.3) did not match the expected result.

Two independent tests by the group verified this.

- **Tilt sensors**

Precise tilt sensors, manufactured by *Wylter* were used to determine the angular discrepancy. These devices of type *Zerotronic inclination sensor* [34] have a high resolution of 8.7  $\mu\text{rad}$  and are therefore ideal to

make this measurement. (Application in the main experiment would be ideal but lack of vacuum compatibility and size prevent this.)

- **Diffraction**

Mounting a grating on the goniometer and shining a laser on it creates a diffraction pattern on a screen at a distance  $L$  ( $= 1$  m). This pattern is perpendicular to the grating slits. A tilt of angle  $\alpha$  of the gratings moves the diffraction pattern by the same  $\alpha$ .

## 5.2 Shaping The Signal

As mentioned in section 4.4.1 the initial signal showed distortions that needed to be resolved. Nevertheless it is possible to extract phase information out of it which will be discussed in section 5.3. Here an overview will be given on the signal shape and the measures taken to improve it.

The signal is given by scanning grating three in the  $z$ -direction. In practice this means step wise acquisition since the actuators do not support linear continuous scanning (see section 4.1). Discrete steps are taken in the  $z$ -direction and at every step the intensity is averaged over  $t = 1$  s. This method eliminates largely the influence of noise on the data. Main contributors to noise is electronic noise in the photo diode (thermal,  $1/f$ ,...) and ambient light. Both setups are inside a box to minimize this effect, but small leaks couldn't be prevented.

As discussed in section 4.3 most of the power is diffracted into 'unused' orders. Therefore the signal amplitude is in the order of  $P_{\text{out}} = 1 \mu\text{W}$ . Furthermore it depends on the position on the grating. This indicates a variance in the open fraction  $\eta$  across the grating. The acquisition electronics has a negative voltage bias of  $V_{\text{Bias}} = -4$  mV giving a constant negative offset to the signal. Back and forth reflections between the aluminium slits and the frame of the grating holders introduced distortions to the signal, as can be seen in figure 5.2a. The reflections accumulate additional phase and therefore manifest as bumps between the main peaks. It is still possible to extract phase information

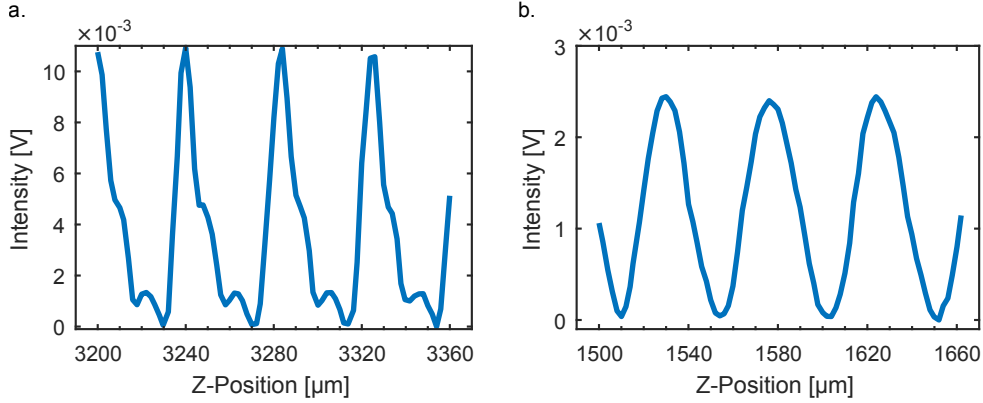


Figure 5.2: Signal shape when scanning grating 3; a. signal including distortions; b. pure signal. The distortions in a. are due to reflections within the setup that accumulate phase. Replacing the aluminium aperture with a non reflective screen cleans up the signal shape.

out of this signal via cross correlation which will be shown in section 5.3. Usage of non reflective black cardboard as screens between gratings gives the expected sine function as shown in figure 5.2b. Here simple curve fitting is sufficient to get the phase information.

### 5.3 Monitoring The Tilt

This section discusses results on tilt monitoring with the concept of the three-beam Mach-Zehnder interferometer. Methods to extract the phase are discussed. This includes cross correlation and fitting. Lastly the minimal achieved resolution is given.

#### Phase Extraction via Cross Correlation

Cross correlation as a means to extract the phase between the two recorded signals is the topic of this sub chapter. Cross correlation is the product of two functions  $f$  and  $g$  as a function of their displacement  $\tau$  between each other

$$(f \star g)(\tau) = \int_{-\infty}^{\infty} f^*(t)g(t + \tau)d\tau . \quad (5.3)$$

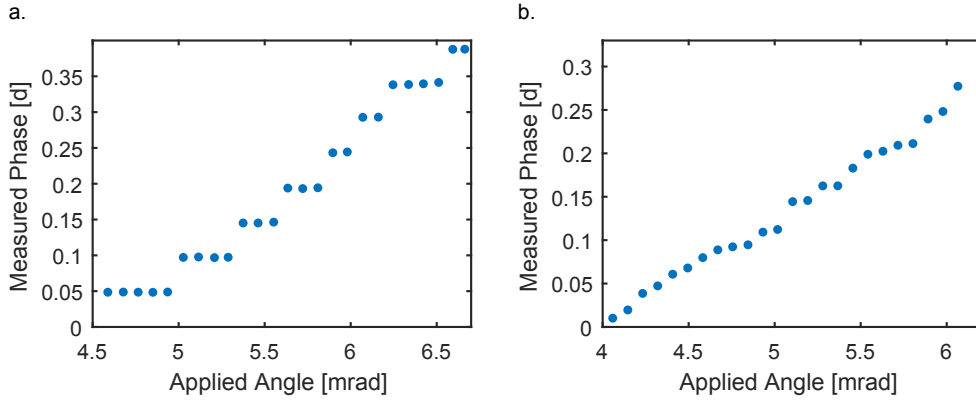


Figure 5.3: Phase difference as function of angle on grating 2; a. sampling of  $2\ \mu\text{m}$ ; b. fine sampling of  $0.5\ \mu\text{m}$ ; each point has been calculated by cross correlation. The step size is linked to the achieved resolution. The discrete steps of  $0.05d$  in a. match the step size of  $2\ \mu\text{m}$ . A smaller step size, as seen in b. with  $0.5\ \mu\text{m}$  improves the resolution.

For discrete functions the integral turns into a sum. As discussed in section 5.2 the signal shape in the initial set up is not a sine function but shows distortions, as can be seen in figure 5.2a. Nevertheless it is still possible to extract phase information out of such a signal as long as the bumps are constant within one full phase. In this case cross correlation proves to be a powerful tool. Here it can be used to find the phase by 'sliding' one recorded signal on top of the other. When the cross correlation function is maximal both signals are in phase. Out of this information the phase shift can be calculated. The results are plotted in figure 5.3. There the phase difference between the 'Left' and the 'Cross' Mach-Zehnder is given as a fraction of the periodicity  $d = 40\ \mu\text{m}$  plotted against the angle of grating two.

The signals recorded during one scan of the third grating is a collection of discrete data points. For such a discrete cross correlation the minimal detectable phase shift is given by the finesse of the sampling. Two signals with different step size in the z-direction are shown in figure 5.3. Fig. 5.3a. is scanned with a step size of  $2\ \mu\text{m}$  and Fig. 5.3b. with  $0.5\ \mu\text{m}$ . The difference in phase resolution is clearly visible. The signal sampled in  $2\ \mu\text{m}$  steps shows a discontinuous behavior. The distance between each jump,  $5\%$  of  $d$ , corre-

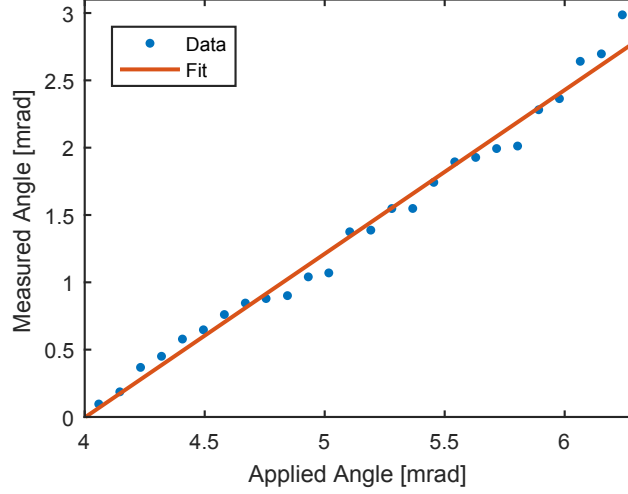


Figure 5.4: Phase evolution as a function of angular difference and linear fit to the data. Data has been recorded with step size of  $0.5 \mu\text{m}$ . The fitted slope is compatible with the expected factor of  $a = 1.2$ .

sponds directly to the  $2 \mu\text{m}$  step size. However the  $0.5 \mu\text{m}$  steps applied in fig. b. give sufficient resolution.

### Applied Angle vs. Measured Angle

The following discussion shows that with a combination of distorted signal and cross correlation the theory described in section 3.3 matches the experimental outcome.

According to equation 3.24 a linear behavior of the phase difference with the angular difference is expected. In the setup given in section 4.4.1 the relevant parameters are the periodicity  $d$  and the distance on the first grating  $h$ :

$$h = 4.2 \pm 0.3 \text{ mm} \quad (5.4)$$

$$d = 40 \mu\text{m} \quad (5.5)$$

A linear fit is done on the data in figure 5.3b. as is shown in figure 5.4. The phase is calculated into the corresponding angle with the parameters given



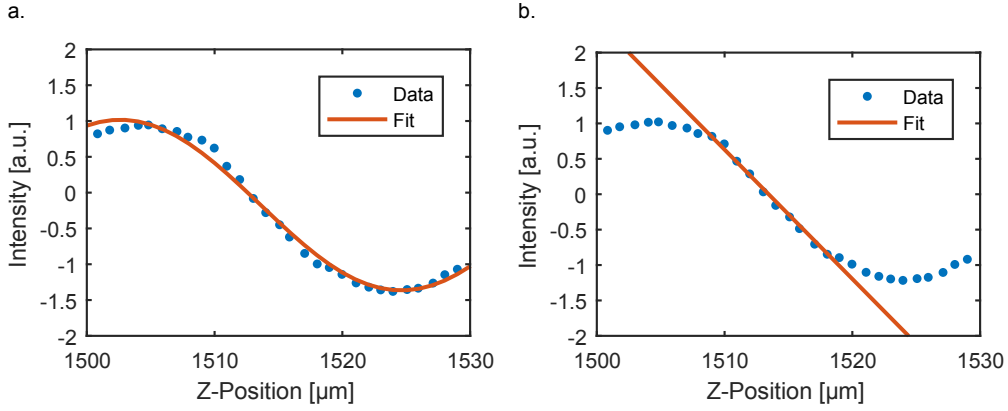


Figure 5.5: Intensity over one scan of third grating. The phases are extracted by fits to same data set; a. sinus fit; b. linear fit. The data in a. is approximated by a sine function. Both approaches are compatible. The linear fit is preferred due to better reliability and smaller fitting errors.

above. The fit gives a slope  $c$  of

$$c = 1.216 \pm 0.030 \quad (5.6)$$

This result is compatible with the measured correction factor  $c_{\text{cor}}$  found in section 5.1.

### Phase Extraction via Fitting

The data presented above has been taken in the initial setup described in section 4.4.1. The main improvement in the second iteration (see section 4.4.2) is the 'clean' signal shape. This means the phase can be extracted by a fitting procedure. In the following discussion both a sine fit as well as a linear fit will be considered. A fitting method is desired compared to the cross correlation discussed above. Such a procedure will require less acquisition of data and will speed up the measuring process.

Figure 5.5 shows two fits on the same data points. An offset has been added to shift the mean to zero. Figure 5.5a. shows a sinusoidal fit while figure 5.5b. shows the linear fit on the maximum slope of the signal. Information on the

phase is encoded in the fitting function  $\sin(\frac{2\pi}{d}(x - \Phi))$  in case a. and in the intersection with the x-axis of  $a(x - \Phi)$  in case b.

Figure 5.5a. reveals that the detected signal is more complex than a sine function. It is skewed in its peaks to one side. This could be due to the gratings themselves.

Using these two approaches to extract the phase difference out of a data set gives compatible results.

### Angular Scans On Translational Stages

With the variable setup described in section 4.4.2 and this method of phase extraction the angles are monitored as before.

Starting with big angular steps of 1.7 mrad the set up is tested. Figure 5.6 shows the behavior of the angular difference between grating 1 and 2 as well as 2 and 3 when grating 2 is tilted. Since both results are extracted from the same grating, both plots must show the same behavior. Indeed linear fits on the evolution in figure 5.6a. and b. gives compatible results within  $3\sigma$ .

$$c_{1,2} = 1.218 \pm 0.041 \quad (5.7)$$

$$c_{2,3} = 1.382 \pm 0.084 \quad (5.8)$$

Notice that these results are compatible within  $3\sigma$  with the correction factor  $c$  obtained in section 5.1. Still,  $a_{2,3}$  is not matching as well as previous results. This could possibly be explained by a misalignment in the intersection plane of 'Right' and 'Cross' beam.

The second data point in figure 5.6b. is significantly off the expected line. This can be attributed to an error during the data acquisition in which the parallel translation of the laser went further than planned. Therefore it has been excluded in the fit.

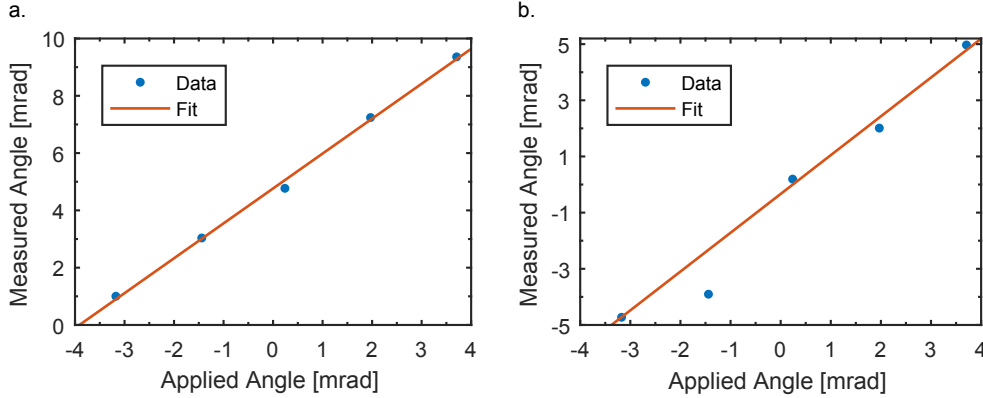


Figure 5.6: Grating 2 is moved by 1.7 mrad in each step. Figure a. shows the measured angle between grating 1 & 2; b. between grating 2 & 3. A linear Fit is added. The second point in b. is due to an error during data acquisition and is excluded from the fit. The slopes are compatible with the expected value of 1.2.

### Fine Angular Scan

After proving the working principle the minimal detectable tilt is tested with this version. In order to get there, the second grating is tilted by  $35 \mu\text{rad}$  in each scanning step. Figure 5.7 shows the extracted angle between grating one and two, both with the sine fit (orange) and the linear fit (blue). The errors are given by the 68% confidence intervals of the fit parameter. Both methods are compatible with each other within  $2\sigma$ . Interestingly there is a systematic offset between both results of  $\alpha_{\text{offset}} = 59 \pm 13 \mu\text{rad}$ . This could be due to the signal shape described above. This skewing of the sine might influence the fit parameter for the phase  $\Phi$ . The error given by the fits is smaller in the linear case. This comes from the reduced number of parameters that need to be considered.

It becomes apparent, that the data in figure 5.7 does not allow reliable reconstruction of the applied angle. A linear fit on the data reveals a trend of

$$c = 1.31 \pm 0.39 \quad (5.9)$$

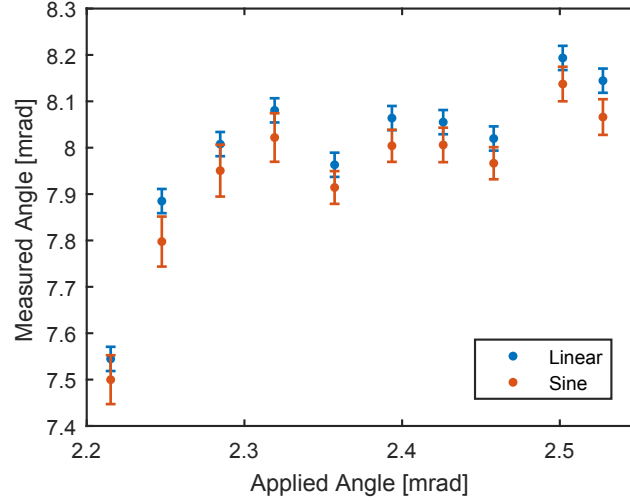


Figure 5.7: Measurement with  $35 \mu\text{rad}$  steps on grating two. The Phases have been extracted by fitting: blue: linear function; orange: sine function. An offset between both methods is visible and due to the skewed signal shape. The data points are not on a line but scatter. The translational stages introduced further uncertainties.

Even though this is compatible in principle, an error of 30% on the slope does not give confidence in the result.

How can this be explained? The idea to move the setup onto translational stages introduced these fluctuations seen in figure 5.7. One data point is taken by three individual scans with translations of the laser in between. In this procedure two effects are possible:

- **Hysteresis:** The actuators of type 'Oriel encoder mike' show most likely a hysteresis effect. This will have an effect on the position and the tilt of the laser beam. Displacements in the plane of grating one or two show up linearly in the measured phase difference. This means a hysteresis effect over time would accumulate linearly.
- **Drifts:** Drifts of the set up are very well possible. The laser out coupler is mounted on a translational stage and has an additional actuator mounted horizontally to introduce a tilt. Also there are cables and a fiber attached which might stress the build during movement. Having

the aperture move over many scans can influence the stability of the position.

Relying on a movable setup is the main reason the angular behavior is distorted. A setup which has all three beams fixed is the main step for the next iteration of this project.

### Achieved Resolution

Lastly the minimal detectable resolution will be given. Even though the last measurement can be labeled as inconclusive, the work presented here can give a few insights on this topic. The combination of both setups presented gives the following result:

A step size of

$$\Delta\alpha = (87 \pm 14)\mu\text{rad} \quad (5.10)$$

$$= (5.0 \pm 0.8)\text{mdeg} \quad (5.11)$$

was resolved. With the correction factor of  $a = 1.2$  the real achieved resolution is:

$$\Delta\alpha = (104 \pm 17)\mu\text{rad} \quad (5.12)$$

$$= (6.00 \pm 0.96)\text{mdeg} \quad (5.13)$$

This is the mean and its standard deviation over all data points presented in figure 5.4.

The results show, that

$$\Delta\alpha_{\text{resolved}} > \Delta\alpha_{\text{crit.}} \quad (5.14)$$

The resolution achieved is not sufficient to meet the requirements for AtliX. Phase extraction via cross correlation is linked to the step size in the z-direction. The  $0.5\mu\text{m}$  steps are sufficient for the resolution given above. Going for a genuine, fixed three-beam Mach-Zehnder will open up the possibility of a slope fit again. This method has potential to give better resolution over a

## 5 Results

---

shorter acquisition time (less periods with less finely sampled data).

## 6 Summary & Outlook

This chapter will give a brief summary of the results as well as an outlook for the steps necessary to implement a fully realized version of this work in the main experiment of AtliX.

### 6.1 Summary

This thesis details work on a system designed to monitor tilts of a Talbot-Lau interferometer consisting of three equidistant gratings. A concept using three independent laser Mach-Zehnder interferometers describes how their mutual phase differences is related to the angular differences between the gratings. In order to achieve this, two setups have been designed as a means to test the theory. For both designs the chosen method for phase extraction is discussed and results for the monitored angle are given. Lastly the minimal achieved resolution is given as

$$\Delta\alpha = (104 \pm 17)\mu\text{rad} \quad (6.1)$$

$$= (6.00 \pm 0.96)\text{mdeg} \quad (6.2)$$

This resolution is bigger than the critical angular difference  $\Delta\alpha_{\text{crit.}}$  for the Talbot-Lau interferometer in AtliX of

$$\Delta\alpha_{\text{crit.}} = 37\mu\text{rad} . \quad (6.3)$$

A static setup is expected to improve the resolution.

### 6.2 Outlook

Following this work it is clear that the next step is to build a setup which mimics the conditions that the final version will work with. This means the full three-beam interferometer with simultaneous readout of all three outputs. In fact at the time of writing work has already begun to realize this. A new

laser is in place that will give more power output to improve the signal. It is a pigtailed laser diode with 70 mW of power at  $\lambda = 638$  nm. The provided laser beam will be split in four parts by a fiber splitter with each at approx. 25 %. Three of the outputs will be collimated and used for each individual interferometer. The fourth can be used to monitor the intensity output of the laser.

The advantages are clear. This system is the complete equivalent to the envisioned implementation in the main experiment. This implementation in the main experiment should be straight forward. However there are some details to consider:

A full version of the work presented here must be operational in vacuum and should not disturb the main experiment of proton interferometry. Vacuum compatibility means the parts used inside the chamber can not outgas (when parts are manufactured with chemicals such as glue). This could potentially effect the vacuum quality. Furthermore any charge up effects between or after the gratings, when the proton beam is on, must be eliminated. This means coating any elements placed inside (such as the screens blocking unwanted diffraction orders) or 'hiding' them in places where contact with protons will not happen.

At the time of writing new gratings have been commissioned with this three-beam interferometer in mind and should arrive soon. Their  $7\text{ mm} \times 7\text{ mm}$  area is divided into an upper and lower part of  $3\text{ mm} \times 7\text{ mm}$  with a 1 mm bar between them. The upper part is a grating with nanometric pitch for the Tolbot-Lau interferometry of protons while the lower part is intended for monitoring of the tilt with the method presented in this work. The advantage of this setup is that the angle between the nanometric and  $40\text{ }\mu\text{m}$  grating is controlled and ideally zero.

The path to a full implementation of angular grating control with a three-beam Mach-Zehnder interferometer is clear and has the potential to improve precision measurements of (anti-) proton interferometry in AtliX.



## References

- [1] L. De Broglie and F. L. de Broglie (Paris), *Recherches sur la théorie des quanta*. Masson Paris, 1963.
- [2] C. J. Davisson, “The diffraction of electrons by a crystal of nickel”, *Bell System Technical Journal*, vol. 7, no. 1, pp. 90–105, 1928.
- [3] O. Carnal and J. Mlynek, “Young’s double-slit experiment with atoms: A simple atom interferometer”, *Physical review letters*, vol. 66, no. 21, p. 2689, 1991.
- [4] B. Brezger, L. Hackermüller, S. Uttenthaler, J. Petschinka, M. Arndt, and A. Zeilinger, “Matter-wave interferometer for large molecules”, *Physical review letters*, vol. 88, no. 10, p. 100404, 2002.
- [5] M. K. Oberthaler and P. Bräunig, “Atlix proposal”, 2014.
- [6] R. Bach, G. Gronniger, and H. Batelaan, “An electron talbot-lau interferometer and magnetic field sensing”, *Applied Physics Letters*, vol. 103, no. 25, p. 254102, 2013.
- [7] S. Gerlich, L. Hackermüller, K. Hornberger, A. Stibor, H. Ulbricht, M. Gring, F. Goldfarb, T. Savas, M. Müri, M. Mayor, *et al.*, “A kapitza–dirac–talbot–lau interferometer for highly polarizable molecules”, *Nature Physics*, vol. 3, no. 10, pp. 711–715, 2007.
- [8] E. Lau, “Beugungserscheinungen an doppelrastern”, *Annalen der Physik*, vol. 437, no. 7-8, pp. 417–423, 1948.
- [9] M. Gruber, K. Eder, A. Zeilinger, R. Gähler, and W. Mampe, “A phase-grating interferometer for very cold neutrons”, *Physics Letters A*, vol. 140, no. 7-8, pp. 363–367, 1989.
- [10] M. Weber, “Gravitation in der interferometrie mit kalten neutronen”, PhD, Innsbruck University, 1998.

## References

---

- [11] G. Y. Drobychev, U Gendotti, I Boscolo, H Walters, M Büchner, A. Rubbia, M. Oberthaler, P Nedelec, S Zavatarelli, C Carraro, *et al.*, “Proposal for the aegis experiment at the cern antiproton decelerator (antimatter experiment: Gravity, interferometry, spectroscopy)”, Tech. Rep., 2007.
- [12] A. Demetrio, “Gravity measurement on h in aegis: Numerical simulation of perturbative effects”, Master’s thesis, Genoa University, 2014.
- [13] P. Bräunig, “Atom optical tools for antimatter experiments”, PhD, Heidelberg University, 2014.
- [14] H. F. Talbot, “Lxxvi. facts relating to optical science. no. iv”, *The London and Edinburgh Philosophical Magazine and Journal of Science*, vol. 9, no. 56, pp. 401–407, 1836.
- [15] S. R. Müller, “Moiré deflectometer for charged particles”, Master’s thesis, Heidelberg University, 2016.
- [16] P Sortais, T Lamy, J Médard, J Angot, L Latrasse, and T Thuillier, “Ultracompact/ultralow power electron cyclotron resonance ion source for multipurpose applications”, *Review of Scientific Instruments*, vol. 81, no. 2, 02B314, 2010.
- [17] G Van der Zouw, M Weber, J Felber, R Gähler, P Geltenbort, and A Zeilinger, “Aharonov–bohm and gravity experiments with the very-cold-neutron interferometer”, *Nuclear Instruments and Methods in Physics Research Section A: Accelerators, Spectrometers, Detectors and Associated Equipment*, vol. 440, no. 3, pp. 568–574, 2000.
- [18] Merriam-Webster, *Merriam-webster’s collegiate dictionary*. Merriam-Webster, 2004.
- [19] E. Hecht, *Optik. 5., verbesserte auflage*. Oldenbourg Verlag, München, 2009.
- [20] K. K. Sharma, *Optics: Principles and applications*. Academic Press, 2006.

## References

---

- [21] A. A. Michelson and E. W. Morley, “On the relative motion of the earth and of the luminiferous ether”, *Sidereal Messenger*, vol. 6, pp. 306–310, 1887.
- [22] B. P. Abbott, R. Abbott, T. Abbott, M. Abernathy, F. Acernese, K. Ackley, C. Adams, T. Adams, P. Addesso, R. Adhikari, *et al.*, “Observation of gravitational waves from a binary black hole merger”, *Physical review letters*, vol. 116, no. 6, p. 061 102, 2016.
- [23] L. Mach, “Über einen interferenzrefraktor”, *Zeitschrift für Instrumentenkunde*, vol. 12, pp. 89–93, 1892.
- [24] L. Zehnder, *Ein neuer interferenzrefraktor*. Springer, 1891.
- [25] O Iwase, W Süß, D. Hoffmann, M Roth, C Stöckl, M Geissel, W Seelig, and R Bock, “Laser-produced plasma diagnostics by a combination of schlieren method and mach-zehnder interferometry”, *Physica Scripta*, vol. 58, no. 6, p. 634, 1998.
- [26] R Chevalerias, Y Latron, and C Veret, “Methods of interferometry applied to the visualization of flows in wind tunnels”, *JOSA*, vol. 47, no. 8, pp. 703–706, 1957.
- [27] G. Van der Zouw, *Gravitational and aharonov-bohm phases in neutron interferometry*. na, 2000.
- [28] P. Bräunig, “High-stability deflectometer for antimatter gravity measurements”, Diploma, Heidelberg University, 2010.
- [29] attocube systems AG. (2016). Product catalog 2016 & 2017.
- [30] F. Laermer and A. Schilp, *Method of anisotropically etching silicon*, 1996. [Online]. Available: <http://www.freepatentsonline.com/5501893.html>.
- [31] F. Bergermann, “Characterization of the moiré deflectometer for the aegis-experiment”, Diploma, Heidelberg University, 2012.
- [32] F. C. Hauptert, “Ein moiré-deflektometer als gravimeter für antiwasserstoff”, PhD thesis, Heidelberg University, 2012.

## References

---

- [33] Thorlabs-GmbH. (2015). Det10a(/m) si biased detector user guide.
- [34] Wyler, *Manual sensor zero-tronic*, 2016.

## **Erklärung**

Ich versichere, dass ich diese Arbeit selbstständig verfasst und keine anderen als die angegebenen Quellen und Hilfsmittel benutzt habe.

Heidelberg, den 06.03.2017,